



HAL
open science

Strain localisation and grain breakage in sand under shearing at high mean stress: insights from in-situ x-ray tomography

M. Gkiousas-Kapnisis, A. Totabi, Gioacchino Cinno Viggiani, E. Ando, Reza Alikarami

► To cite this version:

M. Gkiousas-Kapnisis, A. Totabi, Gioacchino Cinno Viggiani, E. Ando, Reza Alikarami. Strain localisation and grain breakage in sand under shearing at high mean stress: insights from in-situ x-ray tomography. *Acta Geotechnica*, 2015, 10 (1), pp.15-30. 10.1007/s11440-014-0364-6 . hal-01954512

HAL Id: hal-01954512

<https://hal.univ-grenoble-alpes.fr/hal-01954512v1>

Submitted on 9 Jun 2020

HAL is a multi-disciplinary open access archive for the deposit and dissemination of scientific research documents, whether they are published or not. The documents may come from teaching and research institutions in France or abroad, or from public or private research centers.

L'archive ouverte pluridisciplinaire **HAL**, est destinée au dépôt et à la diffusion de documents scientifiques de niveau recherche, publiés ou non, émanant des établissements d'enseignement et de recherche français ou étrangers, des laboratoires publics ou privés.

1 Strain localisation and grain breakage in sand under shearing 2 at high mean stress: insights from *in-situ* x-ray tomography

3 Alikarami R.^{1,2}, Andò, E.³, Gkiousas-Kapnisis M.³, Torabi A.¹, Viggiani G.³

4¹ Uni CIPR, Uni Research , P.O. Box 7810, N-5020 Bergen, Norway

5² Earth Science Departments, University of Bergen, P.O. Box 7800, N-5020 Bergen, Norway

6³ Grenoble-INP / UJF-Grenoble 1 / CNRS UMR 5521, Laboratoire 3SR, 38041 Grenoble, France

7 Corresponding author: Reza Alikarami, Uni CIPR, Uni Research , P.O. Box 7810, N-5020 Bergen, Norway
8 (reza.alikarami@uni.no)

9

10 Abstract

11 This work presents results from a series of triaxial compression tests on two quartz sands
12 (differing principally in grain shape), at confining pressures high enough to cause grain breakage
13 during shearing. Tests are performed inside an x-ray scanner, which allows specimens to be
14 imaged non-destructively as they deform. Observation of the acquired images clearly shows
15 different mechanisms of deformation, including shearing, dilation, compaction and grain
16 breakage. These mechanisms are investigated quantitatively through 3D measurements of local
17 porosity, as well as strain (obtained by 3D Digital Image Correlation), which is analysed in terms
18 of volumetric and shear components. These tools allow the transition between macroscopically
19 dilative (typically of a dense sand at low mean stress) and compactive behaviour to be
20 investigated. The analysis reveals that at the high end of the confining pressure range studied
21 (100 to 7000 kPa) the more rounded sand deforms with highly localised shear and volumetric
22 strain – the porosity fields show a dilative band within which a compactive region (due to grain
23 crushing) grows. The more angular material shows shear strain localisation, however its faster
24 transition to compactive behaviour (due to a higher propensity for individual grains to crush)
25 translates to much more distributed compactive volumetric strain.

26 Keywords

27 Deformation band, Grain breakage, Grain shape (angularity), Triaxial compression test, In-situ x-
28 ray microtomography, 3D Digital Image Correlation

29

301. Introduction

31 Weakly cemented and poorly lithified sandstones are important class of geological reservoirs
32for hydrocarbon production and are good candidates for geological carbon dioxide sequestration
33due to their high porosity and permeability. These highly porous rocks undergo different modes
34of deformation depending on their stress history as well as their lithological and petrophysical
35properties. Strain in such sandstones may localise into thin (mm-scale) planar structures often
36referred to as deformation bands [1-3]. The kinematics of deformation bands always includes
37shear, while the volumetric response ranges from dilative to compactive strain (e.g. [1, 4]). Both
38porosity and permeability are reduced within compaction bands and compactive shear bands, as a
39result of pore-collapse and possible grain breakage [5-7]. In dilative shear bands, porosity
40increases and (depending on pore tortuosity and changes in specific surface area) permeability
41may decrease or increase [8-10]. Extensive experimental work has been carried out to study the
42effects of variables such as stress level, porosity and grain size on localised deformation in well
43lithified and cemented sandstone (e.g. [11-15]).

44 At the micro-scale (i.e. the scale of the grain, for a sandstone), strain corresponds to
45combinations of different mechanisms including grains rearrangement (sometimes referred to as
46“particulate flow”), grain breakage (cataclasis) and cement breakage. A full understanding of
47strain localisation in sandstones requires investigation of these mechanisms, all of which strongly
48depend on grain shape and angularity. Experience and knowledge from our previous work on
49natural compactive shear bands formed in very porous and friable sandstone (e.g., [16, 17]) were
50the motivation to explore the behaviour of sand at high mean stress. In this paper, sand is adopted
51as a model material that allows the investigation (at substantially lower mean stresses than that

52needed for sandstone) of all deformation mechanisms mentioned above at the grain scale – with
53the exception of cement breakage.

54 X-ray tomography is proving to be an ideal tool for the investigation of the micro-
55mechanisms of deformation in sand – for example recent work from Laboratoire 3SR, Grenoble,
56has clearly demonstrated the effect of grain angularity on the macroscopic mechanical behaviour
57of sand as well its effect on the formation and development of shear bands in different types of
58sand [18-20], all this at relatively low mean stress, which rules out grain breakage.

59 A series of dry triaxial compression tests on two different sands has been performed *in-situ*
60(*i.e.* performing x-ray scans at various points throughout loading) inside the x-ray scanner in
61Laboratoire 3SR (Grenoble), at mean stresses up to 7000 kPa – which proves to be high enough
62to cause grain breakage. The two sands tested are both quartz sands, with similar grain size
63distributions but different angularities: Ottawa 50-70 sand (rounded) and Hostun HN31 sand
64(angular).

65 The structure of the paper is as follows: the materials and testing method are first described;
66this is followed by a description of the tests performed. The typical, macroscopic measurements
67obtained from triaxial testing are detailed for all tests. The image processing tools used to make
68micro-scale measurements on the acquired x-ray images are then briefly described. These
69measurements are further used to explain the differences in the macroscopic responses observed.
70The paper closes with a discussion of the results obtained.

712. Experiments

722.1 Materials tested

73 The two different types of sand tested in this work are Hostun HN31 sand and Ottawa 50-70
74sand. Hostun sand is angular siliceous sand (see SEM image in Fig. 1) produced in a quarry close
75to the commune of Hostun in the Rhône-Alpes region of France. The Hostun HN31 sand studied
76in this work [21] is mechanically identical to the “Hostun S28” and “Hostun RF” varieties that
77have been thoroughly studied (e.g. [22]). The Ottawa sand is a rounded siliceous sand (see SEM
78image in Fig. 1), that comes from sedimentary deposits in Ottawa, Illinois (U.S.A.). A particle
79size distribution for both sands is presented in Fig. 2; the values of D_{50} of Hostun and Ottawa
80sands are 338 μm and 310 μm , respectively.

812.2 Experimental setup and testing campaign

82 A series of triaxial tests on small specimens of dry Hostun and Ottawa sands at confining
83pressures ranging from 100 kPa to 7000 kPa have been carried out at Laboratoire 3SR with *in-*
84*situ* x-ray scanning. The specimens used in this work are cylinders of approximately 22 mm
85height and 11 mm diameter, with non-lubricated end platens. Note that from a mechanical
86standpoint, the response obtained with such small specimens compares well to that obtained with
87larger (standard size) specimens (in [23]), as discussed in detail in [24].

88 The triaxial cell has no steel tie-bars to take the return force from the axial compression of
89the specimen; this is instead taken by the cell in tension (see Fig. 3). The absence of steel tie-bars
90allows the specimen to be imaged by x-rays, without disturbance, inside the cell. Two triaxial
91cells were used in this experimental campaign: a high and a low pressure cell, which differ
92principally in the thickness of the wall of the cell, as well as how the confining pressure is
93applied. Both cells are made of PMMA (Plexiglas) which is transparent to visible light as well as

94to x-rays. In the lower pressure cell shown in Fig. 3 (designed for confinements up to 1000 kPa),
95the confining fluid is water, and confining pressure is applied by compressed air (coming from a
96compressor) with a pressure controller, allowing a fine control of the confining pressure. For the
97higher pressure cell, confinement by air is no longer feasible, and so a pump is used; for
98compatibility with the pump, the confining fluid is oil.

99 Given the different confining pressures and fluids, two different membranes have been used
100in this experimental campaign. In the lower pressure tests, a 300 μm thick latex membrane (very
101transparent to x-rays) is used. In the higher pressure tests, however, a 500 μm thick neoprene
102membrane is used – primarily to avoid piercing of the membrane, but also for compatibility with
103the confining fluid. The x-ray absorption of this membrane is considerably higher than the latex
104one, so it is clearly visible in the images coming from x-ray tomography (see Fig. 6).

105 All specimens are prepared by air pluviation into the membrane stretched in a mould, aiming
106for a dense initial packing (this specimen preparation technique has been selected for its
107reproducibility). Once prepared, samples are installed into the triaxial cell with vacuum applied to
108the sample. The cell is then filled with the relevant confining fluid, which is slowly pressurised to
109an initial isotropic state, while the vacuum is released.

110 Each specimen is loaded isotropically until the desired confining pressure is reached, at
111which point deviatoric loading is applied under strain control by shortening the sample axially
112using a domed ram driven up by the loading system. The force required to advance the ram is
113recorded with a load cell, and the displacement of the ram is recorded with an LVDT. The
114specimen is shortened with a displacement rate of 21 μm per minute (corresponding to a nominal
115strain rate of just under 0.1% per minute).

116 At various key points during a test, loading is halted, and a tomographic scan is performed
 117by acquiring 1024 x-ray radiographs of the sample as it is rotated 360° around its vertical axis by
 118the rotation stage visible in Fig. 3. Since the specimens scanned are relatively small, the
 119geometrical zoom provided by the x-ray cone-beam coming from the generator gives a pixel size
 120of 15.6 µm/pixel, meaning that each grain within the specimen (we recall the D_{50} is bigger than
 121300 µm for both sands) is clearly represented. The set of radiographs acquired is then
 122reconstructed (using DigiCT 2.4.2 from Digisens) into a 3D field of the x-ray attenuation inside
 123the specimen.

1243. Macroscopic results of triaxial testing

125 This section presents the macroscopic results coming from the triaxial compression tests
 126analysed in this work (see Table 1).

127**Table 1. Summary of tests analysed in this paper**

Material	Test Name	Confining Pressure	Initial Porosity (before shearing)
Ottawa	OUEA06	100 kPa	32.1%
Ottawa	OHEA03	4000 kPa	29.1%
Ottawa	OHEA01	7000 kPa	27.3%
Ottawa	OHEA02	7000 kPa	28.9%
Hostun	HNEA01	100 kPa	37.7%
Hostun	HHEA03	1000 kPa	33.7%
Hostun	HHEA05	1000 kPa	34.8%
Hostun	HHEA04	2000 kPa	35.1%
Hostun	HHEA06	3000 kPa	34.3%
Hostun	HHEA02	4000 kPa	34.6%
Hostun	HHEA01	7000 kPa	33.8%

128 In some tests, a few scans are performed during the isotropic loading of the specimen,
 129however most are during deviatoric loading. When deviatoric loading is halted to perform a scan,
 130some axial stress relaxation occurs, which can be seen as small drops of deviator stress

131 throughout the q/p vs. ϵ_a responses of both sands (see Figs. 4 and 5 noting that $p = \frac{1}{3}(\sigma_a + 2\sigma_r)$

132 and $q = (\sigma_a - \sigma_r)$ with σ_a and σ_r being the axial and radial stresses respectively).

133 Figures 4 and 5 show the deviator stress response normalised by the mean normal stress (q/p)
134 and volumetric strain response (in %) both against axial shortening (normalised by the initial
135 height) for all the tests on Ottawa and Hostun sands. Since samples are tested dry, the
136 macroscopic measurement of bulk specimen volume that is used to measure volumetric strain is
137 actually derived from the images of the specimen – the technique for making this measurement is
138 detailed in Section 4.1.

139 It is clear from the responses shown for both sands that there is a significant, but progressive
140 change between the macroscopic material response at 100 kPa and 7000 kPa confinements. The
141 triaxial compression behaviour of Ottawa sand (shown in Fig. 4) with increasing mean stress
142 reveals a progressive retardation (with respect to axial shortening) of the peak deviatoric stress as
143 well as a progressive reduction of its value. The difference between the peak deviator stress and
144 the plateau is large at low confinement (test OUEA06), and the difference reduces with
145 increasing confining pressure – as does the normalised q/p value of the plateau. The considerable
146 dilation undergone by the specimen at 100 kPa confinement progressively reduces from 4000 to
147 7000 kPa. Although the volumetric strain curves obtained for the two tests performed at 7000 kPa
148 confinement differ, the response can be seen to be slightly dilatant (compared to test OUEA06 at
149 100 kPa) in both cases.

150 The evolution of the mechanical response of Hostun sand (Fig. 5) with increasing confining
151 pressure has the same sort of evolution as with the Ottawa sand described above (less clear peak
152 stress and increasingly less dilatant behaviour), however, over the same range of confining
153 pressures this evolution appears to be considerably more rapid: a peak in deviator stress is only
154 clearly visible until 3000 kPa confinement – at higher confinement there is no peak, only strain
155 hardening. The volumetric response also displays a good deal more change than for Ottawa sand:
156 the specimen tested at 100 kPa confinement shows clear dilatancy, whereas the one tested at 7000
157 kPa confinement is contractant throughout. The other tests at 1000, 2000, 3000 and 4000 kPa fall
158 in between these two cases. The stress response of HHEA05 (1000 kPa confinement) also reveals
159 a clear peak, yet with a lower dilatancy than HNEA01 at 100 kPa confinement. Stress-strain
160 responses of HHEA04 at 2000 kPa and HHEA06 at 3000 kPa confinement also show peaks but
161 not as clearly marked as for HNEA01 and HHEA05. Their volumetric responses are very slightly
162 dilatant in the case of HHEA04, and slightly contractant for HHEA06. Stress-strain response of
163 sample HHEA02 tested at 4000 kPa confinement reveals no peak, and shows contraction, but to a
164 lesser extent than test HHEA01 at 7000 kPa.

165 During the post-test removal of specimens tested at high pressures, the production of fines
166 was noted when the contents of the membrane was emptied for weighing. The production of fines
167 by grain breakage may well explain the change from dilation to compaction in the macro-scale
168 volumetric responses of these sands (see Figs. 4 and 5).

169 **4. Image analysis**

170 This section briefly outlines the image analysis techniques used to make micro-scale
171 measurements on the various 3D images coming from the tomographic scans during loading. The
172 objective is to use these tools to explain the differences in the macroscopic responses detailed

173above. The 3D images coming from tomography are 16-bit greyscale measuring
1741250x1250x1600 pixels, with a pixel size of 15.6 μm .

175**4.1 Preparation of images for analysis**

176 In order to make micro-scale measurements from the acquired images, the first step is to
177define the domain (within the image) of the solid skeleton to be analysed, so that measurements
178are made only on this part of each image, and that other objects (such as the top and bottom
179platens, as well as the neoprene membranes) are not taken into account. The specimen-platen
180interface is considered to be a plane, which can be tilted with respect to the specimen's axis.
181Given that the platens have a long extent of flat greyscale (as opposed to the sample, which is
182made of grains and pores), this information is incorporated into an automatic procedure which
183automatically detects points on this interface and fits a plane to the two specimen-platen
184interfaces.

185 The shape of the membrane is rendered more complex by the fact that it does not necessarily
186have a uniform thickness (especially once the sample starts to undergo localised deformation);
187consequently, there is no question of manually removing the membrane, especially taking into
188account the large number of 3D images acquired. A specific image processing technique is
189therefore developed to recognise the inner surface of the membrane: for each horizontal slice, 300
190equally-spaced radial profiles are made, centred on the approximate axis of the specimen. As
191illustrated in Fig. 7, the plot of the variance of this profile reveals sharp peaks, corresponding to
192the rapidly changing greyscale values at material interfaces. Each greyscale profile is variance
193filtered and the characteristic peaks are used to identify the border points: a closed border
194defining the inside of the membrane is then created by connecting these 300 individual points by
195linear segments. Finally, a 3D median filter (of radius 5 pixels) is used to smooth out this border.

196The full technique is shown in Fig. 7, and its effectiveness can be seen from the way in which the
197membrane visible in Fig. 6b is removed in Fig. 6c.

198 After each individual stage has been processed, the inside of the specimen is defined with a
199geometrically complex border around the inside of the membrane bounded by two planes. The
200number of voxels (3D pixels) within this space can be counted, using the pixel size, and used to
201calculate the bulk volume of the specimen as imaged.

2024.2 Local measurement of porosity

203 Porosity is a key measurement for granular materials, and its spatial distribution is of
204particular interest given the different volumetric strain responses seen with macro-scale
205measurements. Porosity is defined as the ratio of the volume of voids to the total volume. This
206can be measured locally, by defining a 3D subvolume within a 3D image and measuring the
207volume of the voids within the subvolume. In previous work [26], voids have been counted by
208*binarising* the greyscale 3D image into a black and white image of the solid and void phases by
209applying a threshold. Observation of the images obtained in this work, particularly for Hostun
210sand at high confining pressure and after shearing shows that grain breakage does indeed occur
211(see Fig. 15 for example), and that the finer grains produced can be small compared to the pixel
212size of the images. This smaller grain phase partially fills voxels, and consequently looks like a
213homogeneous material of x-ray attenuation in between grain and void, thus invalidating the
214inherent two-phase hypothesis for binarisation. In this work, the volume of voids in each
215subvolume is calculated on the greyscale (as opposed to binary) 3D images; values of pore and
216grain greyscale are measured manually on a small selection of pores and grains throughout the
217specimen. Any voxel having a greyscale value equal to, or higher than, the grain greyscale value
218identified is 100% solid, and any voxel having a greyscale value equal to, or lower than, the pore

219greyscale value identified is 100% pore. Greyscale values between these two greyscale limits are
220interpolated with a linear relationship.

221 Local measurements of porosity are therefore made by defining local subvolumes, centred on
222a number of regularly spaced nodes. The size of the cubic subvolumes is selected as a reasonable
223trade-off between sensitivity and representativity of the measurement. Subvolume sizes of
224620x620x620 μm and 470x470x470 μm are used to make measurements on Hostun and Ottawa
225sand respectively.

2264.3 Digital Image Correlation (DIC)

227 In order to make measurements of local kinematics between two 3D images of a deforming
228specimen, Continuum Digital Image Correlation, as implemented in Tomowarp by Hall [27], has
229been used to follow regularly-distributed cubic subvolumes between two different greyscale
230images. The method relies on image correlation and attempts to find a pattern (i.e. the greyscale
231inside a given subvolume) extracted in the reference configuration, and looks for this pattern in
232the deformed configuration. When the best matching pattern is found (by optimizing a correlation
233coefficient mapping one image to the other), the displacement of the subvolume is a natural
234output, and is measured to subpixel precision. This gives the displacement of a series of points
235spread throughout the reference configuration, giving therefore, a full-field measurement of the
236kinematics between the two states. By deriving this displacement field, the 3D strain tensor can
237be obtained. The first two invariants of the strain tensor (representing volumetric and shear strain)
238are chosen for display in the results shown in Section 5.

239 Image correlation has an increased probability of making matching errors when a
240considerable amount of grain breakage occurs between steps. This is due to the considerably

241 different patterns from one image to another that naturally make the patterns harder to match. In
242 order to minimize these potential errors, small increments are analyzed in this work. It is worth
243 noting that DIC is used incrementally, i.e. to measure the displacement field from image $i-1$ to
244 image i , rather than from the initial configuration up to image i . This is different from the “total”
245 porosity measurements presented in Section 5.

246 **5. Measurements from image analysis**

247 **5.1 Tests on Ottawa sand**

248 This section uses the 3D images acquired during the different tests on Ottawa sand to
249 investigate the micro-mechanisms at play during triaxial shearing of the specimens tested at 100,
250 4000 and 7000 kPa confining pressure.

251 Figure 8 shows vertical slices from the final states imaged in each test on Ottawa sand
252 analysed in this work. The slices are oriented to contain the axis of the sample and the normal to
253 the single shear band that is apparent in all cases. In all images acquired at high pressure, the
254 membrane and platens have been removed using the technique described in Section 4.1. These
255 images reveal that in OUEA06 a clear dilatant shear band crosses the sample, whereas for the two
256 samples tested at 7000 kPa confinement, a narrow compactive shear band is also visible,
257 containing crushed material. OHEA03 is an intermediate case, i.e. with no change or slight
258 change in porosity inside the shear band.

259 Figure 9 shows the porosity maps obtained for some key steps during the triaxial shearing of
260 three of the specimens. Prior to shearing, all specimens have relatively uniform distribution of
261 porosities ranging from $n=27\%$ to $n=32\%$. Specimen OUEA06 (tested at 100 kPa confinement)
262 presents a clear, dilatant shear band that develops early in the test – at 3.9% axial shortening

263(around the position of the peak stress) localised dilation is visible, with a porosity in the band of
264around $n=46\%$ by the end of the test. OHEA03 (4000 kPa) does not seem to show localised
265changes in porosity at 3.9% axial strain, however around its peak (at 7.7% shortening, which is
266considerably later than OUEA06), localised dilation is visible. This dilative band continues to
267develop with increasing shearing, and becomes more pronounced by the end of the test (reaching
268a value of $n=39\%$). The sample tested at 7000 kPa confinement (OHEA01) has a considerably
269different behaviour, which is captured well by looking at the porosity maps: by the end of the
270test, a band of *reduced* porosity is noticeable, reaching $n=33\%$ (2% lower than the surrounding
271material). Looking back towards the beginning of the test, two mechanisms can be seen: there is a
272clear and relatively uniform densification of the sample between 0 and 4.3% shortening.
273Thereafter, a dilatant shear band is visible at 12.9% shortening (achieving a porosity of $n=36\%$),
274and at 14.3% shortening, *within* this *dilatant* band, a zone of contraction starts to develop at the
275bottom of the band (on the right side of the specimen), and appears to progressively develop
276within the dilatant band as shearing continues: by 17.2% shortening it crosses the entire
277specimen. This contractive band is consistent in space with the zone of crushed material visible in
278Fig. 8.

279 Figure 10 shows the DIC results (vertical sections of the calculated fields of volumetric and
280shear strain) for some selected increments of the three tests analysed. Interestingly, incremental
281volumetric strain fields can reveal mechanisms that changes in total porosity simply are not
282sensitive enough to pick up. While over the peak the volumetric strain fields from DIC merely
283confirm the dilating bands shown by the porosity fields, the increments analysed at the end of the
284tests reveal that as shearing continues, the volumetric strain in the bands of localised shear strain
285either disappears (for the test at lowest confinement) or becomes compactive (in all the other

286tests), likely due to grain breakage. The shear strain fields show that in all tests the shear band
287gets thinner after the peak.

288**5.2 Tests on Hostun sand**

289 Figure 11 shows vertical slices from the final states imaged in each test on Hostun sand
290analysed in this work. The slices are oriented to contain the axis of the sample and the normal to
291the single shear band (when this is apparent).

292 As for Ottawa, in all images acquired at high pressure, the membrane and platens have been
293removed using the technique described in Section 4.1. These images reveal a range of final states
294that go from a high porosity band (at 100 kPa and to a lesser extent at 1000 kPa confinement) to a
295wide band with clear evidence of crushed grains (in the tests at 4000 and 7000 kPa). The tests at
2962000 kPa and 3000 kPa confinement are intermediate cases, with no striking changes in porosity
297throughout the specimen.

298 Figure 12 shows the porosity maps obtained for some key steps during the triaxial shearing
299of the specimens of Hostun sand. Prior to shearing, all specimens have relatively uniform
300distribution of porosities ranging from $n=27\%$ to $n=32\%$, with initial porosity generally
301decreasing with increasing confining pressure, as expected. Specimens HNEA01 and HHEA05
302both exhibit a clear shear band that becomes increasingly dilatant with increasing shortening –
303with the out-of-band material remaining at almost constant porosity. Specimen HHEA04 tested at
3042000 kPa confinement seems to deform with essentially no porosity change. A progressive and
305distributed reduction in porosity is evident in all specimens tested at higher cell pressure.
306Specimen HHEA02 shows some degree of localisation in porosity reduction at the end of the test.

307 Figure 13 shows the DIC results (vertical sections of the calculated fields of volumetric and
308 shear strain) for some selected increments of the three lower pressure tests. At 100 kPa and 1000
309 kPa confinement, (shear and volumetric) strain localisation starts in a wide band and then
310 progressively concentrates with increasing axial shortening. At 2000 kPa, the shear strain
311 concentrates in a similar fashion, while the maps of incremental volumetric strain confirm that
312 little or no volume changes occur during (progressively localised) shearing. The DIC results for
313 the other three tests analysed (shown in Fig. 14) show that a shear band eventually forms in all
314 tests – which was not evident from either x-ray images or the porosity maps. The reason for this
315 can be seen in the volumetric strain increments presented, which show no localisation. It is also
316 important to note that at these levels of confinement, volumetric strain is essentially compactive
317 rather than dilative – consistent with the global volumetric strains shown in Fig. 5.

318 6. Discussion and conclusions

319 The range of cell pressures used in this experimental campaign has resulted in a significant
320 evolution of the mechanical response of both tested sands, at the macroscopic level. The
321 tendency for increasing confinement is for the volumetric response to change from dilative to
322 contractive, and for the peak of the deviator stress to become less pronounced. This is entirely
323 consistent with previous experimental findings (e.g. [28-30]), all of which attribute this change in
324 macroscopic behaviour to the appearance of grain crushing with increasing mean stress – which
325 is supported by post-mortem sieve analyses.

326 Grain crushing is generally studied through its numerous effects at the macro scale (e.g. its
327 effect on compressibility, shear strength, permeability, etc.). In this work, the process of grain
328 crushing is approached experimentally at the scale of the grain. X-ray micro tomography allows
329 imaging of this process, which is a major mechanism of inelastic deformation in sand at high

330pressure – along with granular rearrangement. Furthermore, the comparison of successive pairs of
331x-ray images (with 3D DIC) yields 3D (incremental) strain fields, which reveal the nature of the
332strain occurring between the two states.

333 In all the tests performed on Ottawa sand, shear strain and volumetric strain are observed to
334localise into a band a few grains thick. At high pressure, grain crushing only occurs in the shear
335band when a sufficiently high porosity is reached. It should be mentioned that this evolution is
336well portrayed by the first three stages (dilation, pore collapse and grain size reduction) in the
337sequence suggested by Lothe *et al.* [30] to describe the evolution of deformation bands in
338sandstones.

339 DIC measurements in Hostun sand show that while shear strains localise in a shear band at
340all pressures, volumetric strain is localised when dilatant (at low pressures) and becomes
341increasing less localised in the contractive regime. X-ray images show diffuse breakage at high
342pressure, with the relatively wide regions of porosity reduction corresponding in space to regions
343of crushed grains (see Fig. 15).

344 Since both Ottawa and Hostun are quartz sands with similar grain size distribution, the cause
345of their different responses can be mainly ascribed to the shape of their grains (rounded in the
346former and angular in the latter). One may hypothesise that in the more angular material the
347amount of energy required to break a grain is lower due to the presence of sharper contacts that
348concentrate stresses on the grain. Therefore, for a given stress level one would expect more
349crushing in the angular material – which is exactly what is observed. The massive grain crushing
350observed in Hostun sand at 7000 kPa confinement suggests that the material is close to the stress
351conditions required for distributed grain breakage. In Ottawa sand, even at 7000 kPa confinement

352breakage only occurs after a strong reduction of porosity, which for a given stress increases
353interparticle forces – this happens only inside the narrow compactive shear band of localised
354strain (see Fig. 15). These differences manifest themselves in the macroscopic response of the
355two sands, most evidently in their volumetric response – with the specimens of Ottawa sand
356never showing overall compaction whereas Hostun crosses this threshold between 2000 and 3000
357kPa confinement.

358 The findings of this study on sand highlight the central role played by grain shape on both
359the stress level needed to break grains as well as the patterns of deformation (localised vs.
360diffuse). It is the authors' contention that these findings are also largely applicable to poorly
361lithified sandstones. These results are of particular interest for hydrocarbon production and CO₂
362storage in sandstone, where the overall reservoir permeability and its evolution is key for the rate
363at which extraction/injection processes can occur. In the triaxial compression tests analysed in
364this work, similar materials differing only by the shape of their grains exhibited very different
365distributions of particle breakage, diffuse in the angular material and highly localised in the
366rounded one – with obvious implications for the permeability and its directional variation. The
367stress paths encountered in a natural reservoir are clearly quite different from triaxial
368compression, however one might expect grain shape to play an equally important role under any
369deviatoric stress path, such as those induced by oil production or CO₂ injection.

370**Acknowledgments**

371 This study is part of the IMPACT Project, a consortium R&D project 207806, at the Centre
372for Integrated Petroleum Research (Uni CIPR), Uni Research, funded by the Research Council of
373Norway and Statoil. The authors would like to thank Alessandro Tengattini for his help in the
374quantitative analysis and interpretation of the test results.

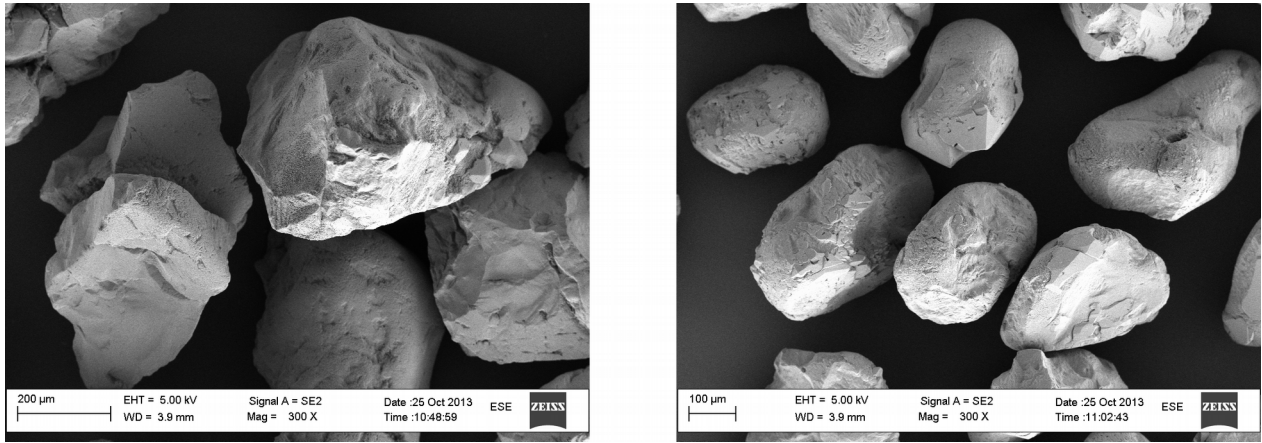
375References

3761. Schultz RA, Siddharthan R (2005) A general framework for the occurrence and faulting of
377deformation bands in porous granular rocks. *Tectonophysics*, 411:1–18. doi:
37810.1016/j.tecto.2005.07.008
3792. Fossen H, Schultz RA, Shipton ZK, Mair K (2007), Deformation bands in sandstone: A
380review. *J Geol Soc* 164:755-769. doi: 10.1144/0016-76492006-036
3813. Torabi A, Berg S (2011) Scaling of fault attributes: A review. *Mar Pet Geol* 28(8):1444-1460.
382doi: 10.1016/j.marpetgeo.2011.04.003
3834. Vajdova V, Baud P, Wong T (2004) Permeability evolution during localized deformation in
384Bentheim sandstone. *J Geophys Res* 109:B10406. doi: 10.1029/2003JB002942
3855. Antonellini M, Aydin A (1994) Effect of faulting on fluid flow in porous sandstones;
386petrophysical properties. *AAPG Bull* 78:355-377.
3876. Torabi A, Fossen H, Alaei B (2008) Application of spatial correlation functions in permeability
388estimation of deformation bands in porous rocks. *J Geophys Res* 113:B08208. doi:
38910.1029/2007JB005455
3907. Aydin A, Berryman J (2010) Analysis of the growth of strike-slip faults using effective
391medium theory. *J Struct Geol* 32:1629-1642. doi: 10.1016/j.jsg.2009.11.007
3928. Cashman S, and Cashman K (2000) Cataclasis and deformation-band formation in
393unconsolidated marine terrace sand, Humboldt County, California. *Geology* 28(2):111-114. doi:
39410.1130/0091-7613(2000)28<111:CADFIU>2.0.CO;2
3959. Du Bernard X, Eichhubl P, Aydin A (2002) Dilation bands: A new form of localized failure in
396granular media. *Geophys Res Letters* 29(24):2176. doi: 10.1029/2002GL015966
39710. Sulem J, Ouffroukh H (2006) Shear banding in drained and undrained triaxial tests on a
398saturated sandstone: Porosity and permeability evolution. *Int J Rock Mech Min Sci* 43:292-310.
399doi: 10.1016/j.ijrmms.2005.07.001

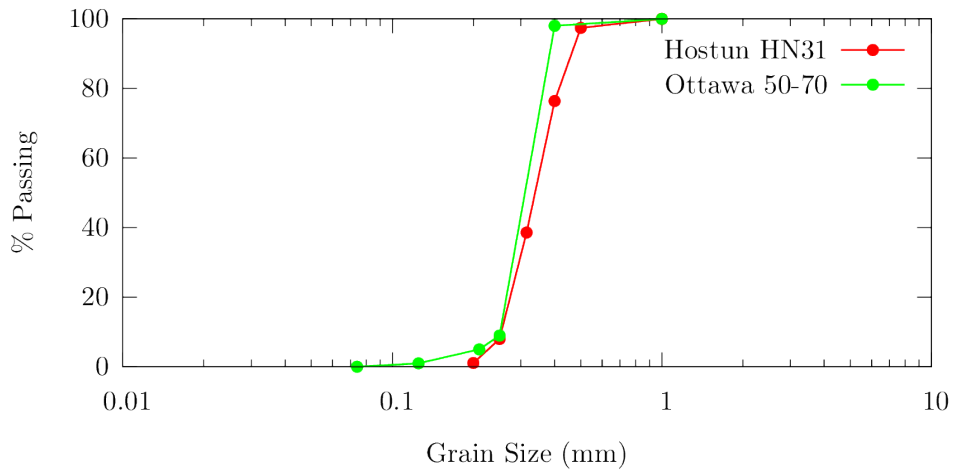
40011. Wong T, David C, Zhu W (1997) The transition from brittle faulting to cataclastic flow in
401porous sandstone: Mechanical deformation. *J Geophys Res* 102:3009-302.
402doi: 10.1029/96JB03281
40312. Bésuelle P (2001) Compacting and dilating shear bands in porous rocks: Theoretical and
404experimental conditions. *J Geophys Res* 106:13435–13442. doi: 10.1029/2001JB900011
40513. Baud P, Klein E, Wong T (2004) Compaction localization in porous sandstones: Spatial
406evolution of damage and acoustic emission activity. *J Struct Geol* 26:603-624. doi:
40710.1016/j.jsg.2003.09.002
40814. Fortin J, Stanchits S, Dresen G, Gue'guen Y (2006) Acoustic emission and velocities
409associated with the formation of compaction bands. *J Geophys Res* 111:B10203. doi:
41010.1029/2005JB003854
41115. Wong T, Baud P (2012) The brittle-ductile transition in porous rock: A review. *J Struct Geol*
41244:25-53. doi: 10.1016/j.jsg.2012.07.010
41316. Torabi A (2014) Cataclastic bands in immature and poorly lithified sandstone, examples
414from Corsica, France. *Tectonophysics*, <http://dx.doi.org/10.1016/j.tecto.2014.05.014>.
41517. Torabi A, Zarifi Z (2014) Energy release rate for propagating deformation bands and their
416hosted cracks. *International Journal of Rock Mechanics and Mining Sciences* 67, 184-190.
41718. Andò E, Hall SA, Viggiani G, Desrues J, Bésuelle P (2012a) Grain-scale experimental
418investigation of localised deformation in sand: a discrete particle tracking approach. *Acta*
419*Geotechnica* 7:1-13. doi: 10.1007/s11440-011-0151-6
42019. Andò E, Hall SA, Viggiani G, Desrues J, Bésuelle P (2012b) Experimental micromechanics:
421grain-scale observation of sand deformation. *Géotechnique Letters* 2:107-112. doi:
42210.1680/geolett.12.00027
42320. Andò E, Hall SA, Viggiani G, Desrues J (2013) Experimental micro-mechanics of granular
424media studied by x-ray tomography: recent results and challenges. *Géotechnique Letters* 3:142-
425146. doi: 10.1680/geolett.13.00036

42621. Sibleco France (2011) Fiche Technique Type HN31. available at:
427http://www.sibelco.fr/item_img/medias/images/ft12_hn31.pdf
42822. Desrues J, Viggiani G (2004) Strain localization in sand: an overview of the experimental
429results obtained in Grenoble using stereophotogrammetry. *Int J Numer Anal Meth Geomech*
43028(4):279–322. doi: 10.1002/nag.338
43123. Colliat-Dangus JL, Desrues J, Foray P (1988) Triaxial testing of granular soil under elevated
432cell pressure. In: Donaghe RT, Chaney RC, and Silver ML (Eds) *Advanced triaxial testing of*
433soil and rock, ASTM STP 977, American Society for Testing and Materials, Philadelphia, pp
434290-310
43524. Andò E (2013), PhD Thesis, Experimental investigation of micro-structural changes in
436deforming granular media using x-ray tomography, Université de Grenoble
43725. Kim HK, Santamarina J (2008) Sand–rubber mixtures (large rubber chips). *Canadian*
438*Geotechnical Journal* 45(10):1457–1466. doi: 10.1139/T08-070
43926. Hall SA, Bornert M, Desrues J, Pannier Y, Lenoir N, Viggiani G, Bésuelle P (2010) Discrete
440and continuum analysis of localised deformation in sand using X-ray μ CT and volumetric digital
441image correlation. *Géotechnique* 60:315–322. doi: 10.1680/geot.2010.60.5.315
44227. Hall SA (2006) A methodology for 7D warping and deformation monitoring using time-lapse
443seismic data. *Geophysics* 71(4):O21–O31. doi: 10.1190/1.2212227
44428. Miura N, Yamanouchi T (1973) Compressibility and drained shear characteristics of a sand
445under high confining pressures. *Technology reports of the Yamaguchi University* 1(2):271 -290
44629. Zoback MD, Byerlee JD (1976) Effect of high-pressure deformation on permeability of
447Ottawa sand. *AAPG Bulletin* 60(9):1531-1542
44830. Lothe AE, Gabrielsen RH, Bjørnevoll HN, Larsen T (2002) An experimental study of the
449texture of deformation bands: effects on the porosity and permeability of sandstones. *Petroleum*
450*Geoscience* 8:195–207. doi: 10.1144/petgeo.8.3.195

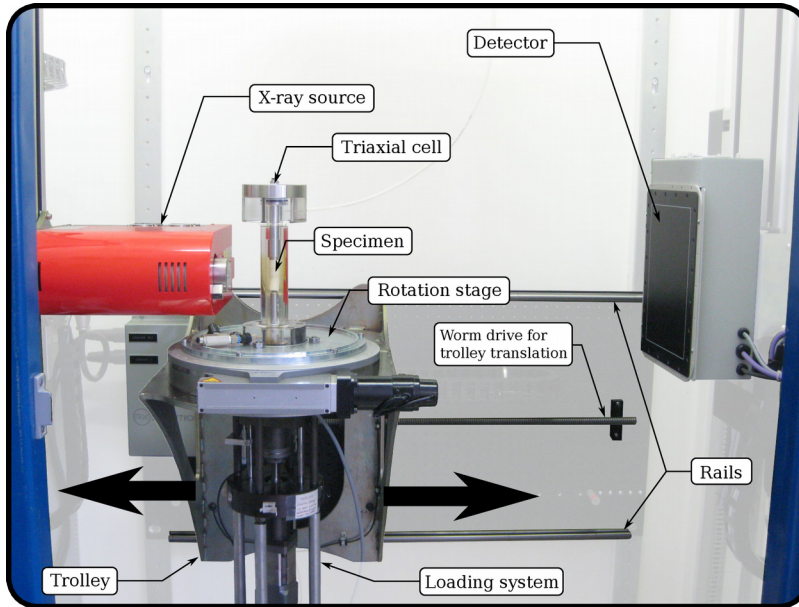
451**Figures**



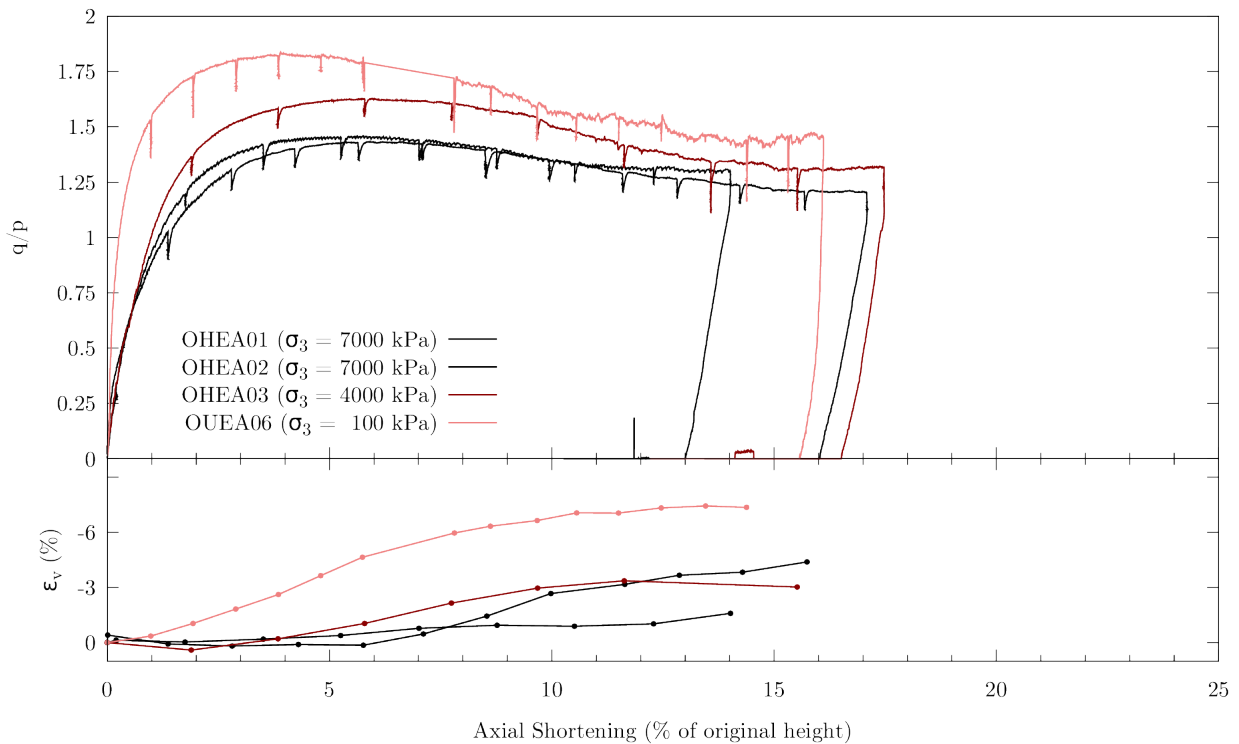
452**Fig. 1** Scanning Electron Microscope (SEM) images of: left) angular Hostun sand grains, and
 453right) rounded Ottawa sand grains



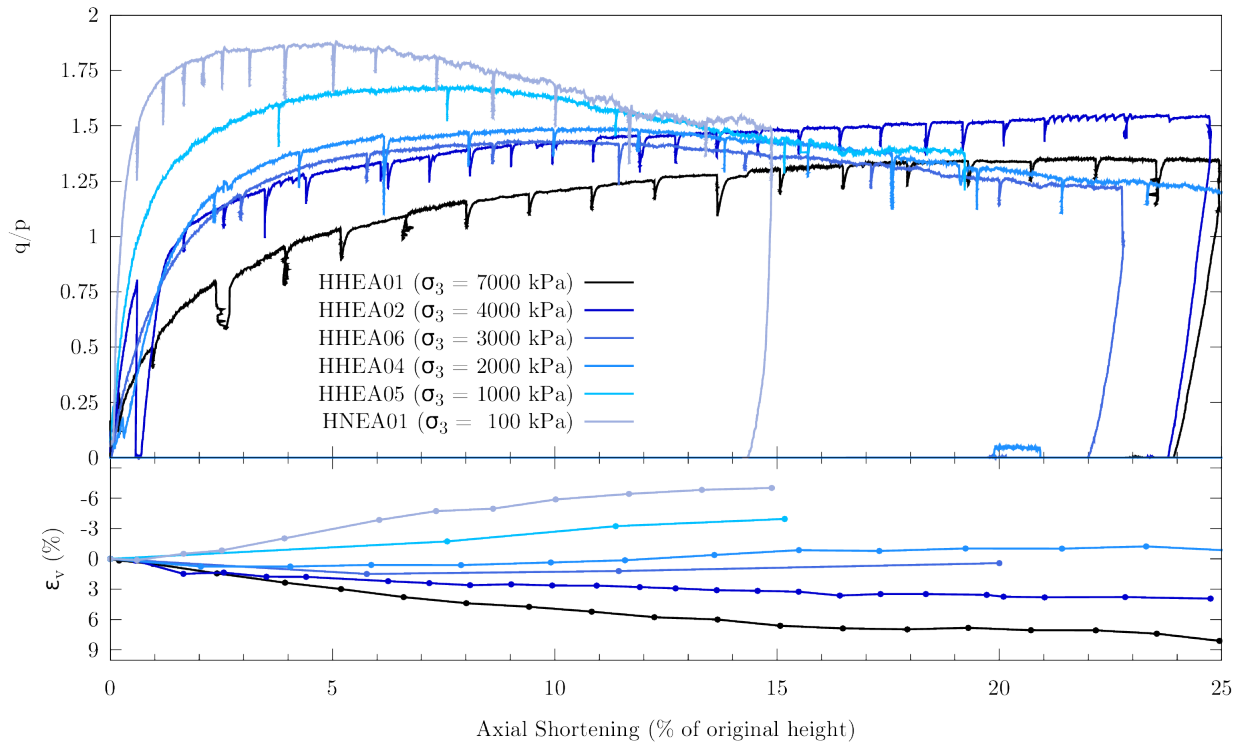
454**Fig. 2** Grain size distribution curves for the two sands studied in this work. Data for Hostun sand
 455comes from the manufacturer [21], and data for Ottawa sand from Kim and Santamarina [25]



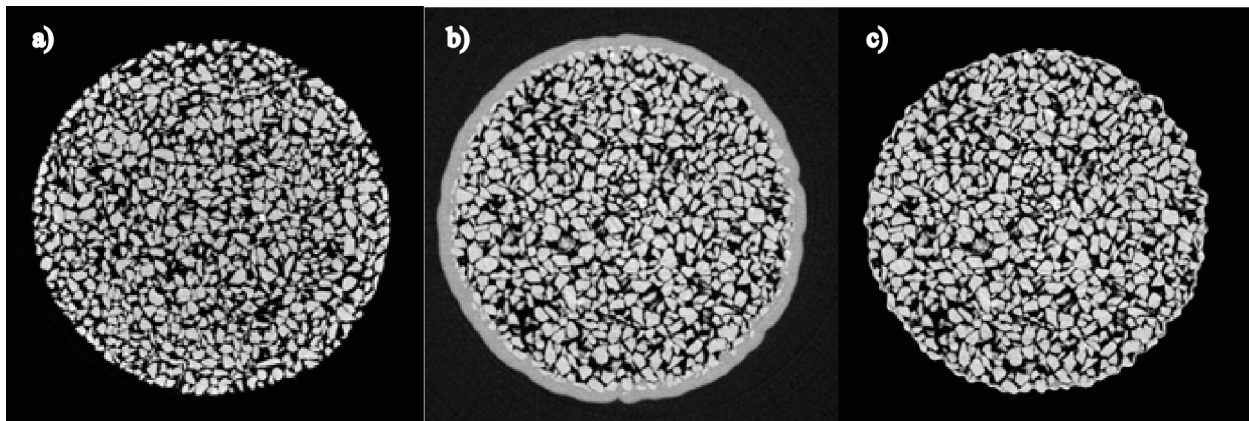
456**Fig. 3** Labelled photograph of the Laboratoire 3SR x-ray scanner, with background faded out for
 457clarity



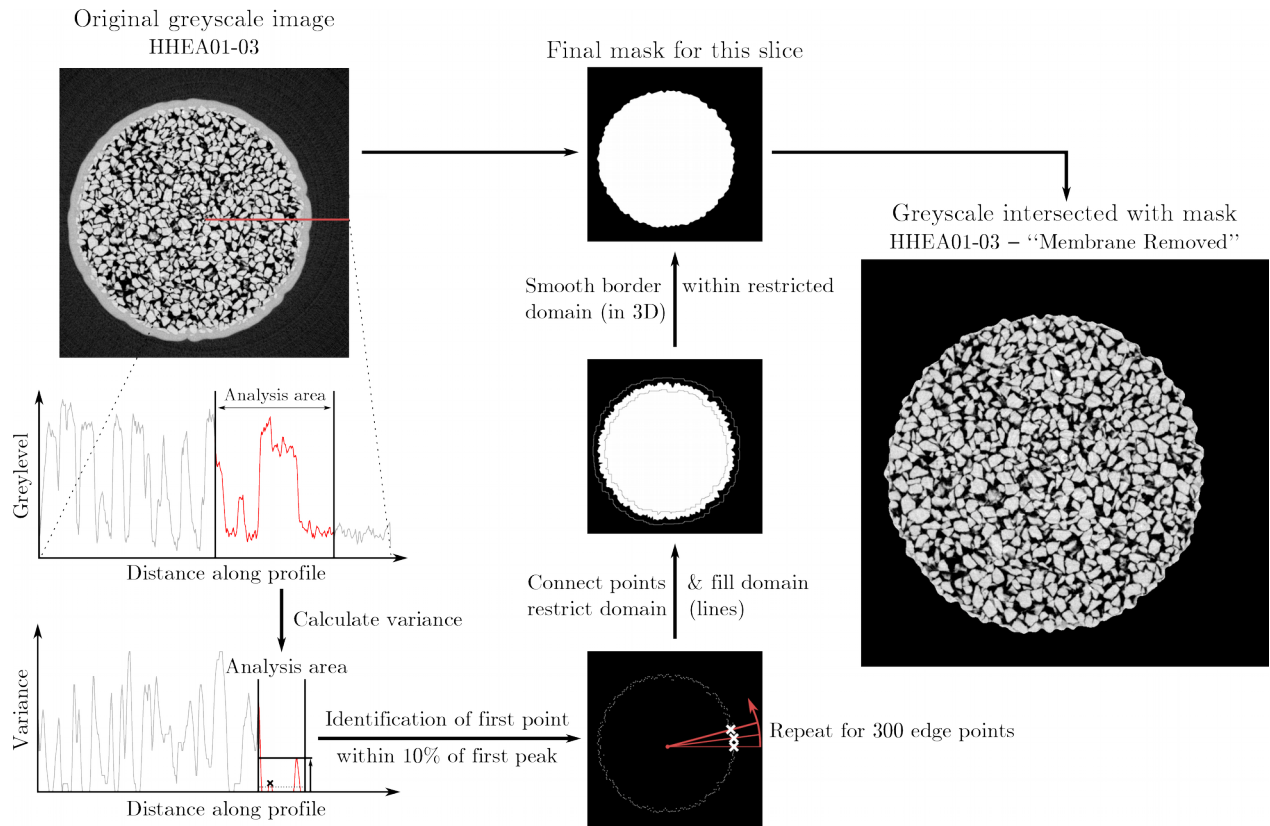
458**Fig. 4** Deviatoric stress normalised by the mean stress (q/p) vs. axial shortening (top) and
 459volumetric strain vs. axial shortening (bottom) for triaxial compressions tests on Ottawa sand



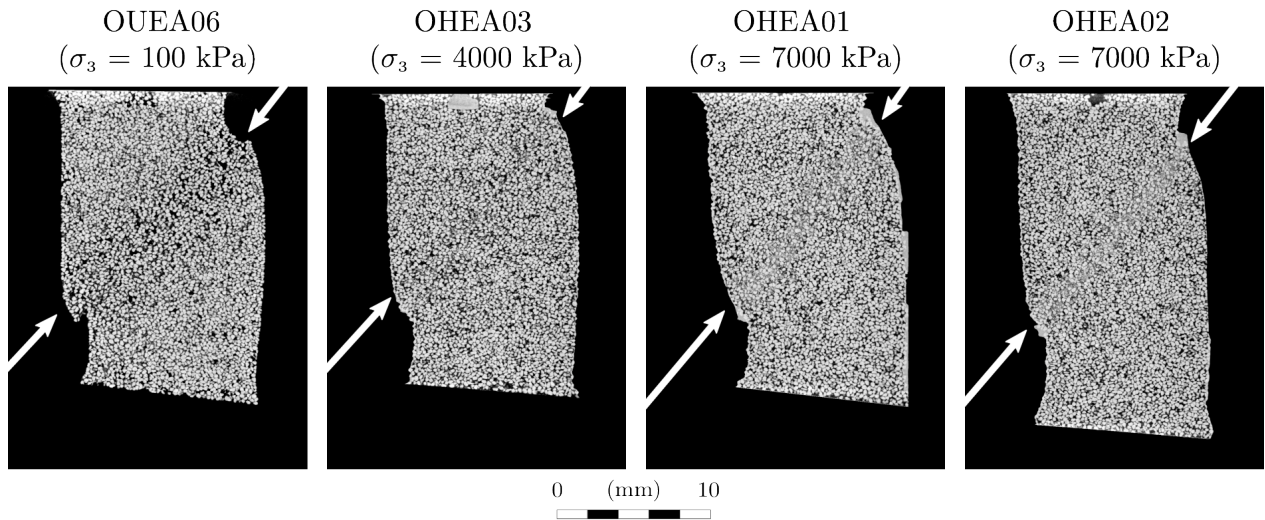
460**Fig. 5** Deviatoric stress normalised by the mean stress (q/p) vs. axial shortening (top) and
 461volumetric strain vs. axial shortening (bottom) for triaxial compressions tests on Hostun sand



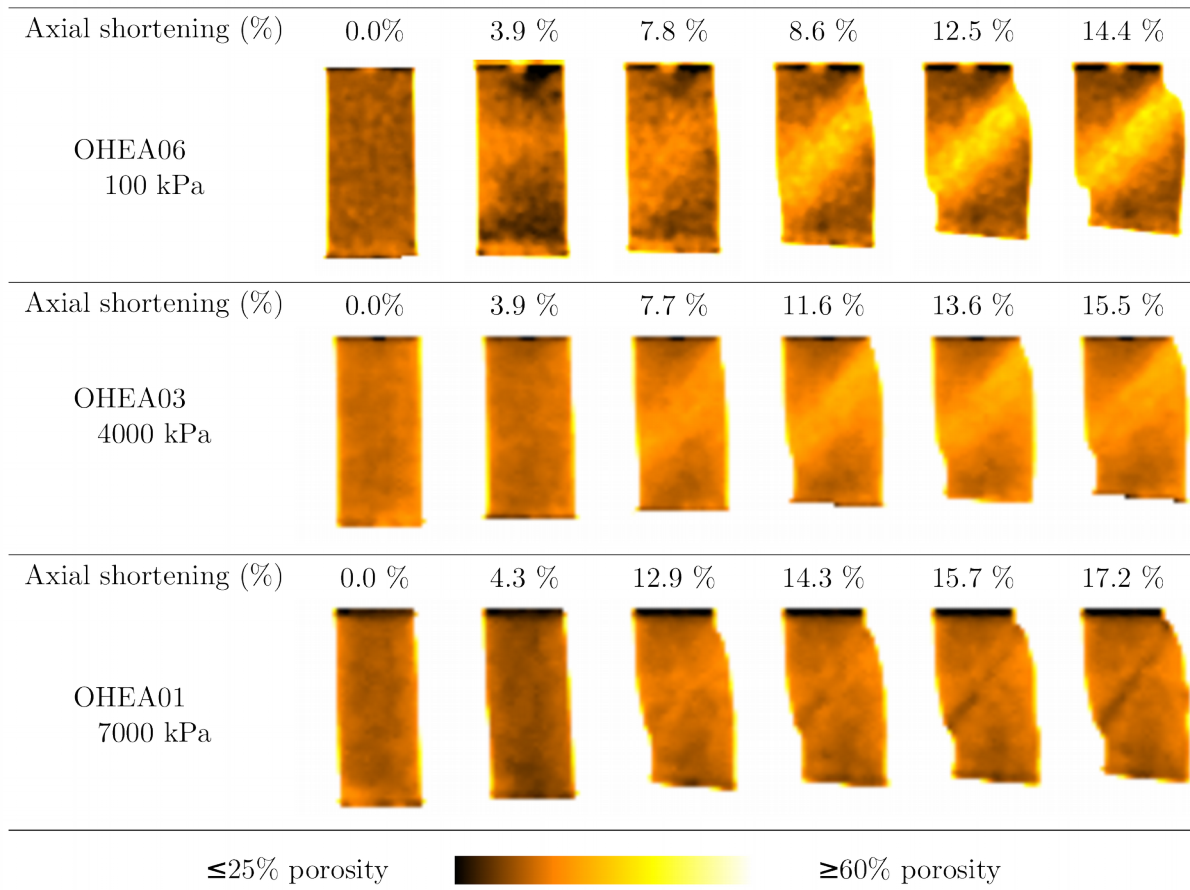
462**Fig. 6** Horizontal slice of a specimen of Hostun sand a) under low confining pressure, b) and c)
 463under high confining pressure but before and after membrane removal, respectively



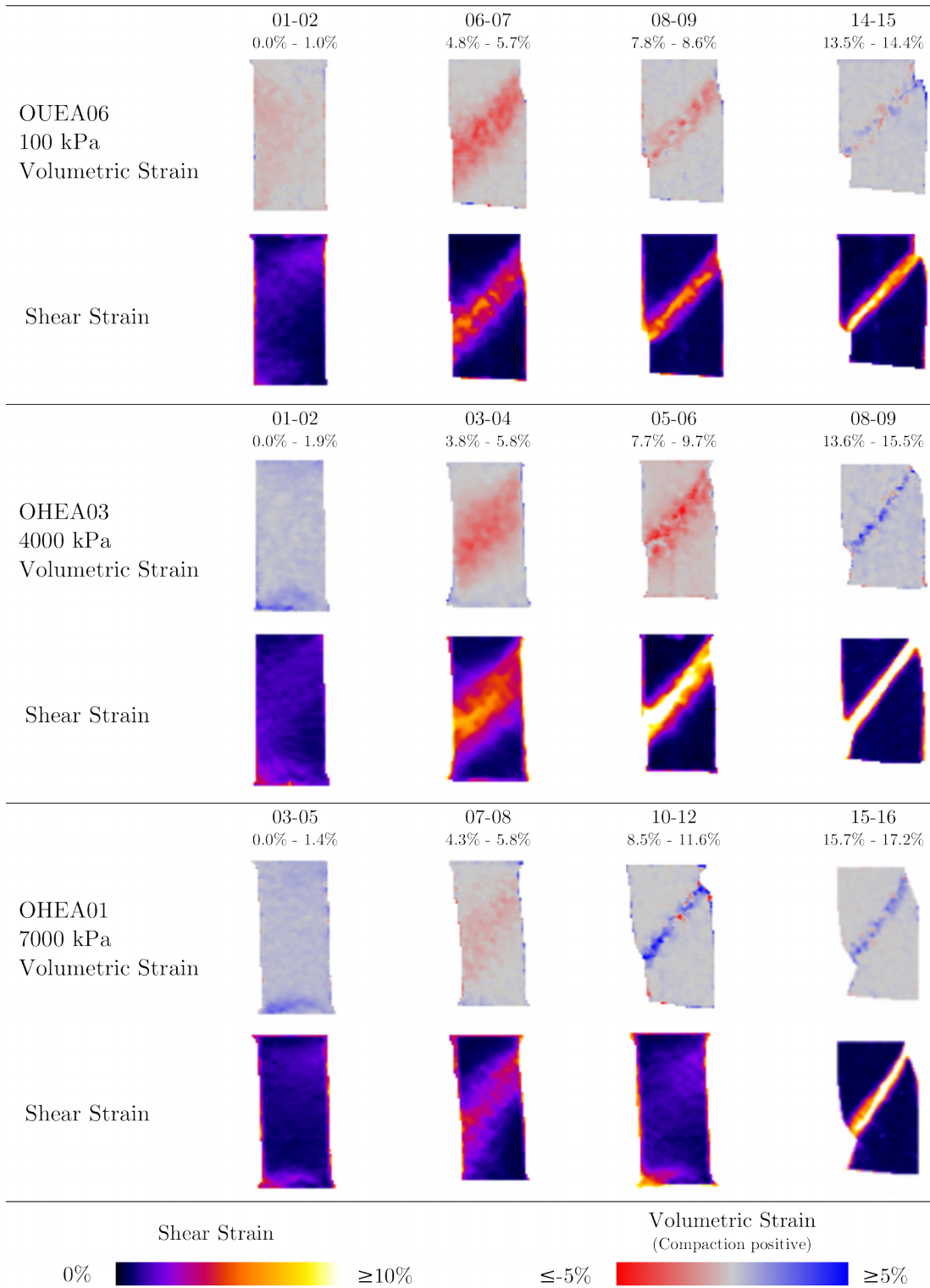
464**Fig. 7** Illustration of the technique developed for the identification and removal of the membrane
 465from the 3D images acquired with the high pressure cell setup



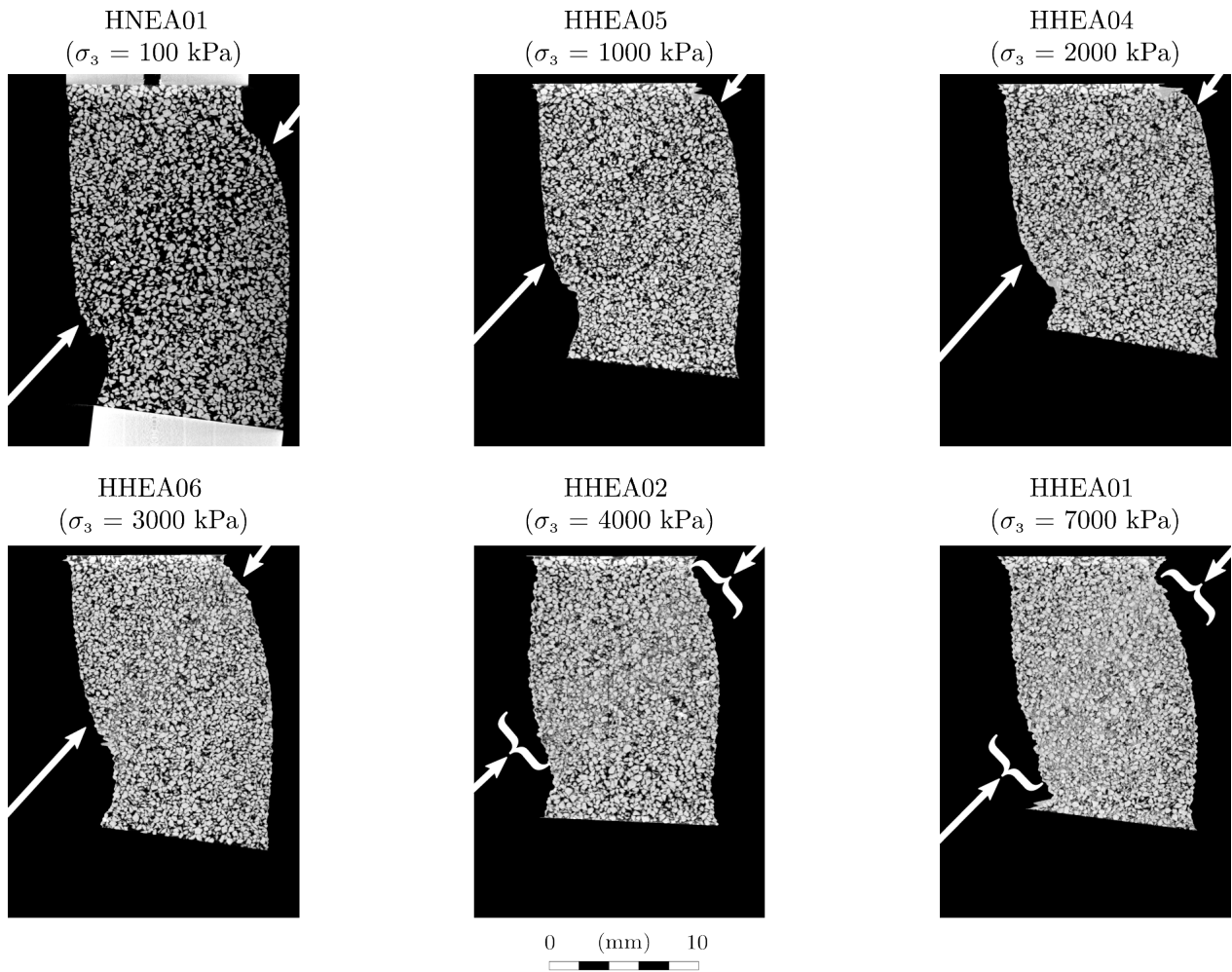
466**Fig. 8** Vertical slices through the last image acquired in each test on Ottawa sand



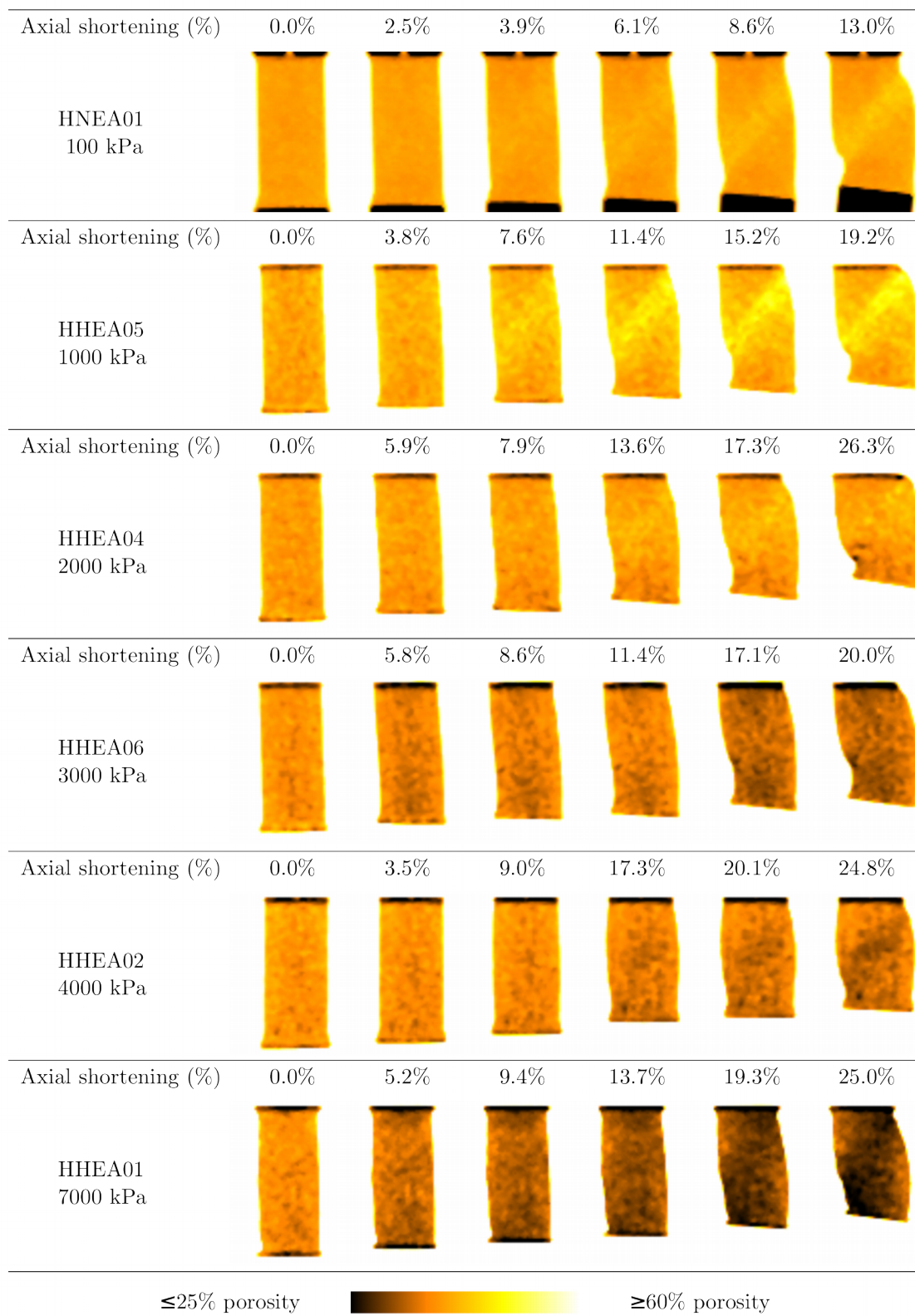
468**Fig. 9** Porosity maps of some selected states of the specimens of Ottawa sand during shearing



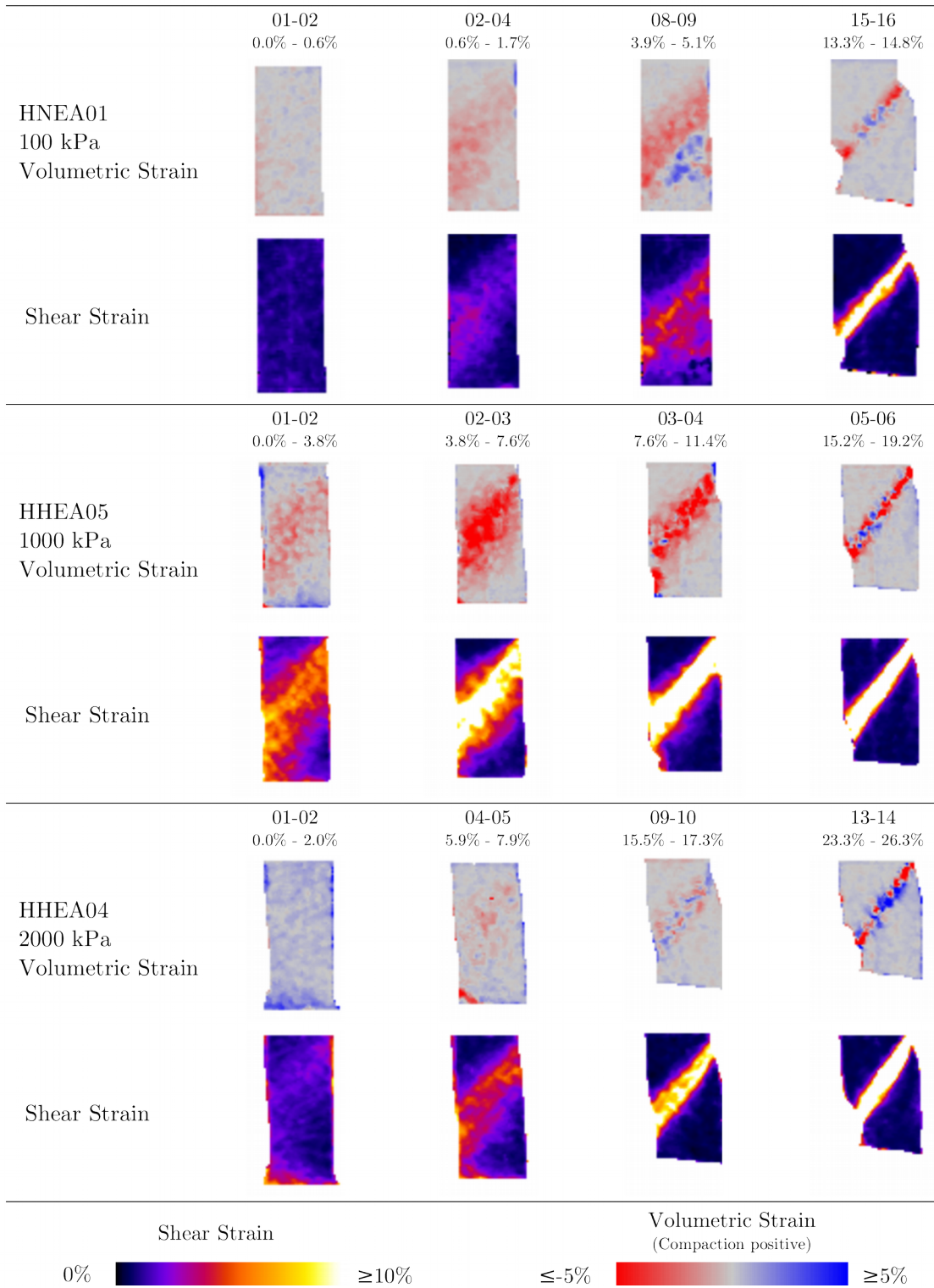
469**Fig. 10** DIC Results for OUEA06, OHEA03 and OHEA01



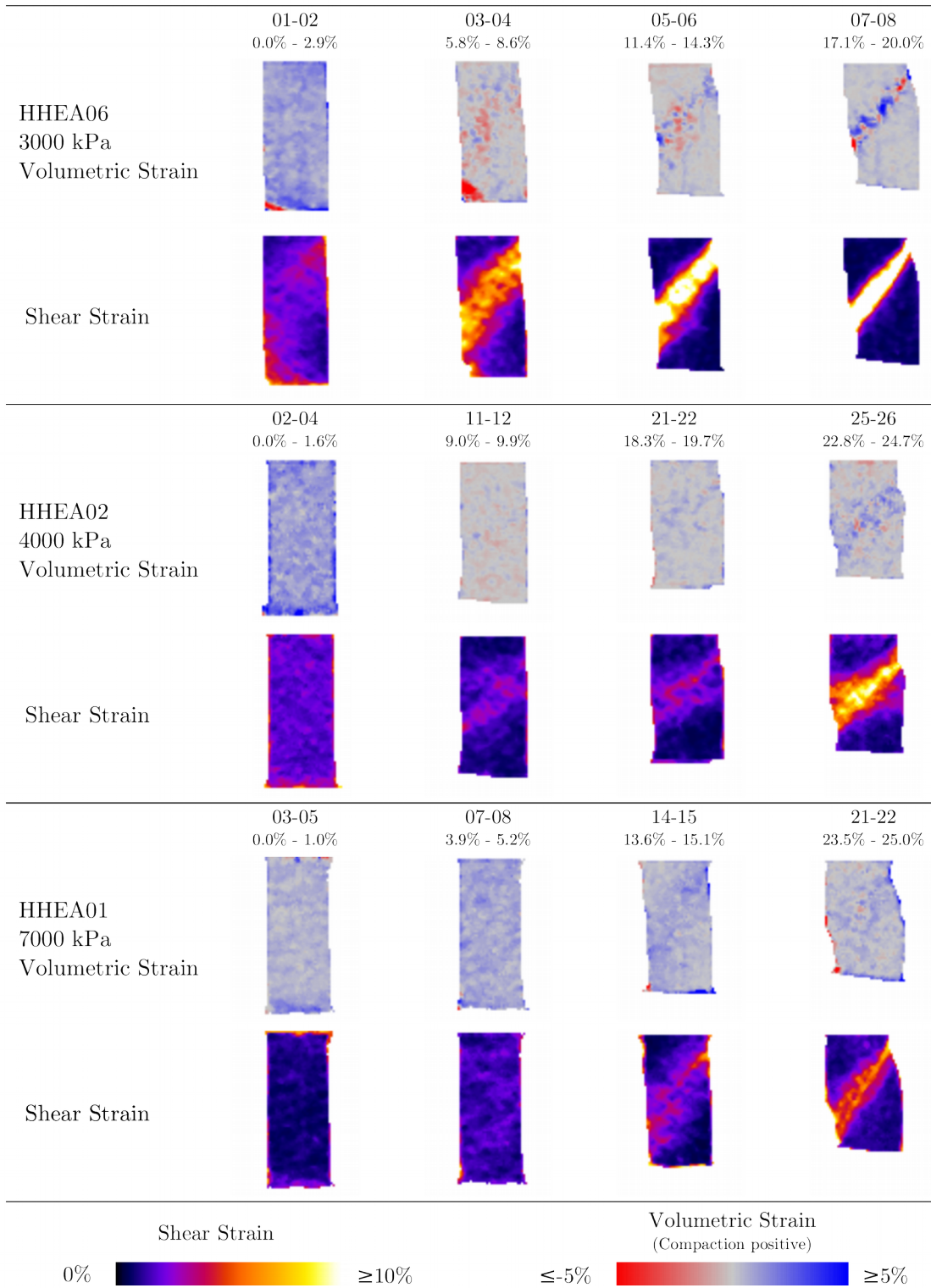
470**Fig. 11** Vertical slices through the last image acquired in each test on Hostun sand



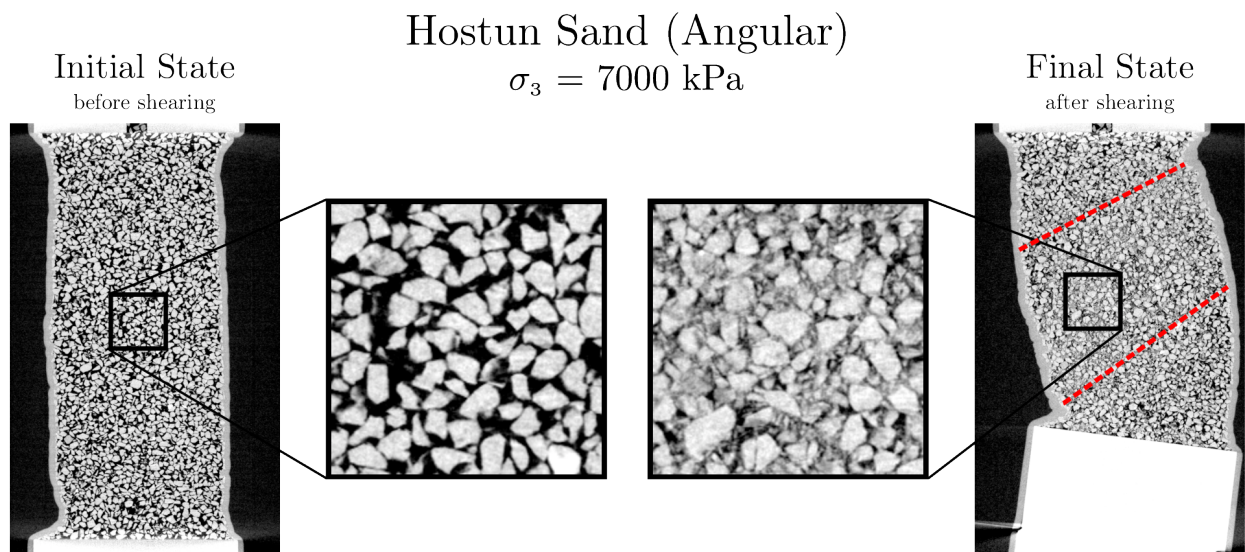
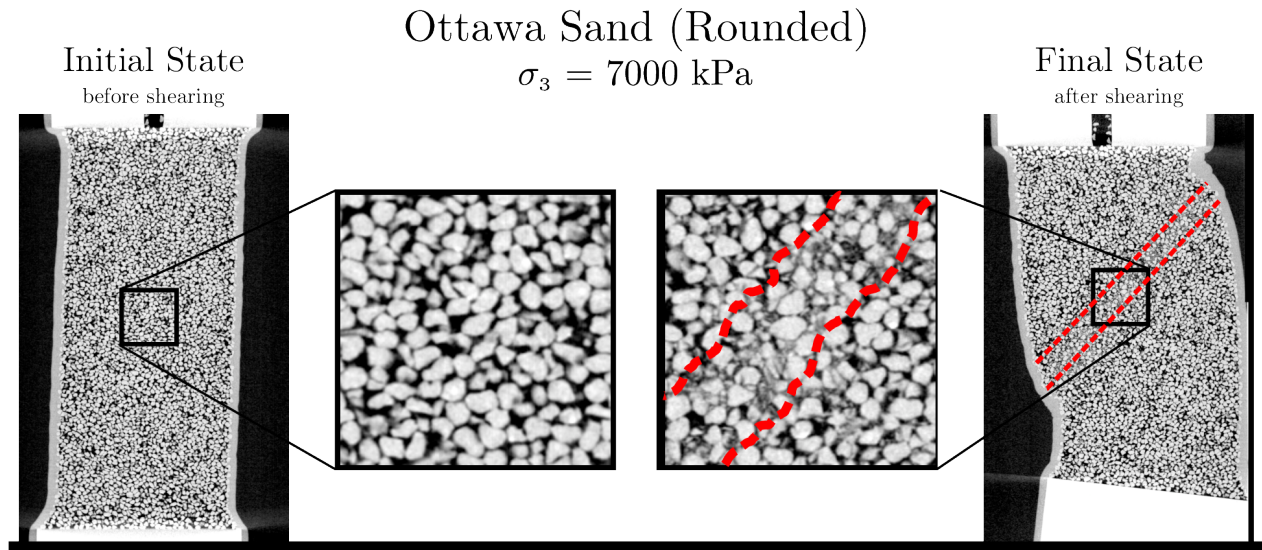
471Fig. 12 Porosity maps of some selected states of the specimens of Hostun sand during shearing



472**Fig. 13** DIC Results for tests HNEA01, HHEA05 and HHEA04



473**Fig. 14** DIC Results for tests HHEA06, HHEA02 and HHEA01



474**Fig. 15** Vertical sections of Hostun and Ottawa sands (under 7000 kPa confinement) with
 475highlighted zones of intense grain crushing.